



Corrosion-resistant metallic coatings for aluminum alloys by cold spray



Chathuranga S. Witharamage ^a, Mohammed A. Alrizqi ^{a,b}, Jijo Chirstudasjustus ^a, Ahmed A. Darwish ^a, Troy Ansell ^c, Andy Nieto ^c, Rajeev K. Gupta ^{a,*}

^a Department of Materials Science and Engineering, North Carolina State University, Raleigh, NC 27695, USA

^b Department of Mechanical Engineering, Jubail University College, Jubail Industrial City, Saudi Arabia

^c Department of Mechanical and Aerospace Engineering, Naval Postgraduate School, Monterey, CA 93943, USA

ARTICLE INFO

Keywords:

Cold spray
Supersaturated solid solution
Supersonic particle deposition
Metallic coating
Sacrificial coating
Aluminum alloys

ABSTRACT

An Al-V alloy powder produced by high-energy ball milling has been cold sprayed on an AA2024-T3 substrate. The corrosion resistance of cold sprayed alloy, represented by the corrosion current density and pitting potential, was significantly higher than the substrate. Furthermore, a zero-resistance ammeter test revealed that the coating was anodic to the substrate, which would provide cathodic protection in any event of coating breakdown. The wear resistance of the coating was almost four times higher than that of the substrate.

1. Introduction

Commercial Al alloys such as AA2024 and AA7075 exhibit a high strength-to-weight ratio and have been a choice of material for lightweight vehicles. However, the poor corrosion resistance of these Al alloys restricts their applications and longevity. Organic [1–3] and conversion [4–9] coatings combined with corrosion inhibitors are used to achieve adequate corrosion resistance in these alloys. However, many corrosion inhibitors are carcinogenic [10–12], and alternative environmentally friendly options are being explored [9,13–15]. Furthermore, organic coatings are prone to mechanical damage because of poor wear resistance, and their applications at elevated temperatures are limited. Metallic coatings are an alternative option. Thermal spray [16–18], chemical vapor deposition [19], and cold spray [20] have been used to produce metallic coatings and improve the mechanical and corrosion properties of the substrate. Cold spray (CS) is a relatively new technique for applying metallic coatings and gaining widespread interest.

Cold spray is a solid-state additive manufacturing process invented as a surface treatment method in the early 1990s [21,22]. The ability to operate at relatively lower temperatures is a unique feature of CS technique, which retains the initial microstructure and properties of the substrate and feedstock [23]. Al [24–30], Cu [31–33], Ni [31,34,35], and Ti [36] based alloys have been used as feedstock materials for CS coatings. These coatings are reported to be compact and possess

excellent adhesion strength and high residual compressive stress at the surface. CS has been used to enhance mechanical properties such as fatigue resistance [30], hardness [37], and wear resistance [38] of alloys by depositing various coating materials. Severe plastic deformation of the particles during the CS process was attributed to the improved mechanical properties of these coatings. In Al alloys, mechanical properties have been significantly improved even though the feedstock was the same as substrate materials [25,39–41]. For example, the deposition of AA6082 alloy powder on the AA6082 substrate revealed a 14.7 % enhancement in fatigue limit compared to the original substrate [41]. Furthermore, the relationships among CS processing parameters, microstructural changes, and properties improvement have been reviewed in [23,42,43]. Additionally, CS has been used to repair damaged components in aircraft [44–48].

The effect of CS on the microstructure and mechanical properties has been widely investigated. However, studying the corrosion behavior of cold-sprayed Al alloys has attracted limited attention [25,28,49–51]. For example, Balani et al. reported the effect of carrier gas on the corrosion properties of cold-sprayed AA1100 [25]. The corrosion resistance in H₂SO₄ with a pH of 0.9 increased due to CS process. Moreover, the corrosion resistance of CS AA1100 produced using He-20 vol% N₂ as carrier gasses was considerably higher than that produced using pure He. The reduced corrosion resistance in the sample produced using pure He was attributed to the higher number of active corrosion sites due to severe plastic deformation. Pure Al has been used as a coating material

* Corresponding author.

E-mail address: rkgupta2@ncsu.edu (R.K. Gupta).

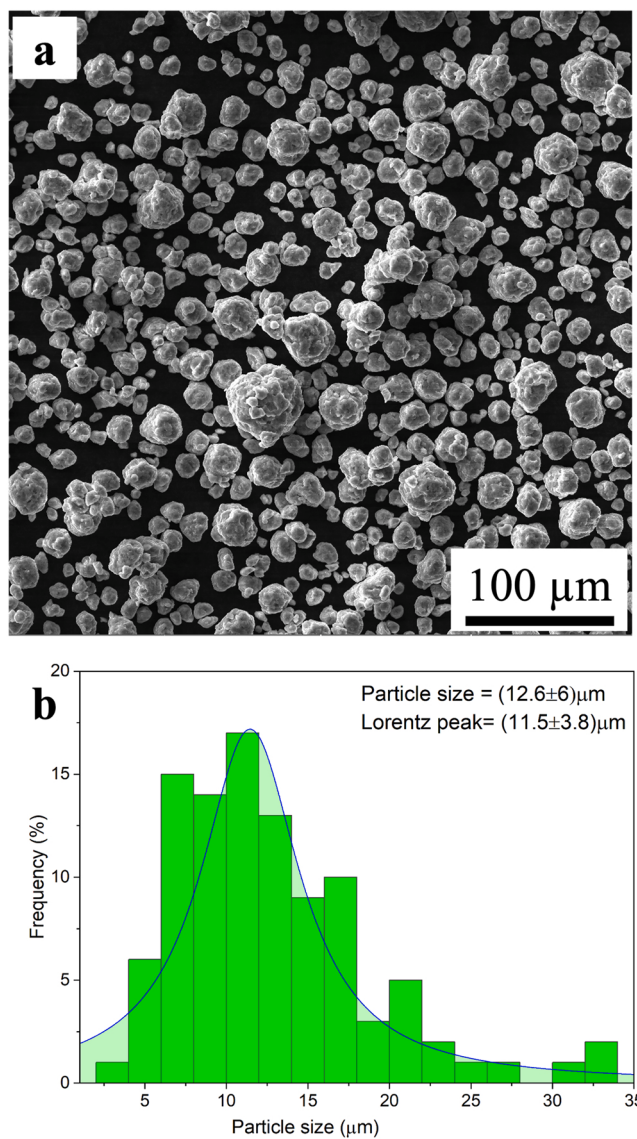


Fig. 1. Morphology of HEBM Al-5at%V alloy powder (Feedstock powder) a) BSE image of powder, revealing shape of particles, and b) Powder particle size distribution estimated using Image J software.

for several high-strength Al alloys [28,52,53]. However, corrosion resistance and mechanical properties such as wear resistance of most Al-coated alloys have been similar to that of pure Al. Corrosion-resistant materials such as Cr, stainless steel, and Ni-based alloys could be used as feedstock to develop corrosion-resistant coatings for Al alloys; however, galvanic interaction between the coating and the substrate in the event of coating breakdown is a great challenge. Therefore, applying a corrosion-resistant coating material, which can act as an anode to the substrate, is critical to protect the alloy from galvanic corrosion.

Recently, Al-M (M: V, Cr, Mo, Ni, Ti, Nb, Ta) alloys produced by high-energy ball milling (HEBM) showed excellent corrosion resistance, strength, and elastic modulus [54–61]. The solid solubility of the alloying elements in these Al-M alloys was several orders of magnitude higher than that predicted by the equilibrium phase diagram [62]. In addition, several Al-M alloys showed corrosion potential similar to commercial Al alloys, which could minimize the galvanic interaction between the coating and the substrate if Al-M alloys are used for coatings. Since Al-M alloys are in a metastable state, CS could retain high solid solubility and grain refinements in the coating, which is expected to result in high corrosion-resistant coatings. In this work, ball-milled

Al-5at%V alloy powder was cold sprayed on an AA2024-T3 substrate. The microstructure and corrosion behavior of cold-sprayed alloys were investigated using various characterization and electrochemical techniques.

2. Methods

2.1. Synthesis of alloy powder and coating using cold spray

Al-5at%V alloy powder was synthesized in a planetary ball mill using steel balls and jars. Elemental powders of Al and V were starting material, and a ball-to-powder ratio of 16:1 was maintained. Jars were loaded inside the glove box (Oxygen < 25 ppm), and 1.5 wt% stearic acid was added as a process controlling agent. HEBM was performed at 280 RPM for 40 h with a pause of 30 min after each hour of milling. The choice of the milling parameters was based on the author's previous work, where milling time and speed were optimized to attain the highest solid solubility of V in Al-5at%V alloy [60]. Properties and microstructure of the ball milled Al-5at%V alloy have been studied in our previous work, where the alloy showed high hardness [55–58,60,63], high corrosion resistance, good thermal stability [58,62], and high elastic modulus [64].

A Centerline Limited Supersonic Spray Technologies (SST) spray division (LaSalle, Ontario, Canada) Series EP low-pressure CS machine equipped with SST X Feeders was used to deposit the Al-5at%V alloy coatings onto the AA2024-T3 substrate. Al-5at%V alloy powder was kept in an oven at 90 °C for 12 h to remove moisture before spraying. AA2024-T3 substrate was cleaned and grit blasted with ~40 μm alumina media to improve the adhesion between the substrate and the coating. Spraying was conducted using a nozzle standoff distance of 12.7 mm, with a raster speed of 40 mm s⁻¹ and a line spacing of 1 mm. The feed rate was 5 %, corresponding to ~4.1 g m⁻¹. Nitrogen gas was used as the carrier gas and was pressurized to 1.65 MPa and heated to 425 °C. CS coating was deposited using two consecutive passes. AA2024-T3 with CS Al-5at%V coating is termed as CS-Al-5 V herein.

2.2. Characterization

2.2.1. Scanning electron microscopy and energy-dispersive X-ray spectroscopy

The scanning electron microscopic (SEM) images of the top surface and the cross-section of CS Al-5at%V (CS-Al-5 V) were obtained using FEI Verios 460 L at 20 kV accelerating voltage. Secondary electrons and backscattered electrons analysis (BSE), along with energy dispersive x-ray spectroscopic (EDXS) elemental mapping were performed on each sample to understand the microstructure and the corrosion of the coating. A Cu layer with a thickness of (15 ± 1.5) μm was electro-deposited on the CS-Al-5 V coated sample (excluding immersion test specimens) prior to the cross-sectional sample preparation. The cross-section was grounded using SiC sandpapers from P400 to P1200 mesh. After that, the specimens were polished up to 0.05 μm surface finish using colloidal silica suspension (particle size of 0.05 μm), followed by ultrasonic cleaning in ethanol for 10 min.

2.2.2. Scanning/transmission electron microscopy

The microstructure of CS-Al-5 V alloy was analyzed using a Talos F200X G2 scanning/transmission electron microscope (S/TEM). The instrument was operated at 200 kV during the experiment. Initially, CS-Al-5 V cross-section was grounded using SiC sandpapers from P400 to P1200. Then the specimen was polished up to 0.05 μm surface roughness using a diamond suspension and subsequently ultrasonicated for 10 min in ethanol. The focus ion beam (FIB) instrument was utilized to prepare the TEM sample using the lift-out technique. To protect the specimen from ion irradiation during FIB, a first Pt layer using an electron beam with a thickness of 300 nm was deposited on the interested region, followed by a second Pt layer using an ion beam with a thickness of 500

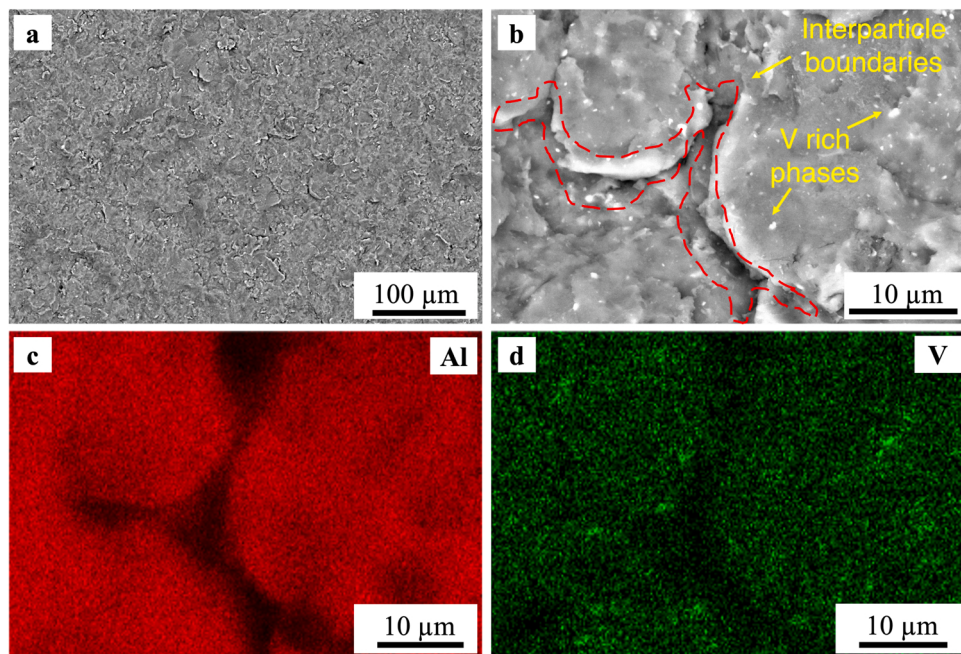


Fig. 2. Microstructural characterization of the surface of CS-Al-5 V using SEM a) BSE image of the top surface of CS-Al-5 V, b) High magnification image showing the morphology of the coating, including interparticle boundaries and V-rich phases, c) and d) EDXS elemental Al and V mapping of (b).

nm. The specimen was thinned to below 100 nm, which is ideal for the TEM investigation. High-angle annular dark field (HAADF) STEM and bright-field (BF) STEM images were acquired to study the microstructural features. In addition, EDXS elemental mapping was performed to understand the elemental distribution.

2.2.3. X-ray diffraction

The parallel beam X-ray diffraction (XRD) analysis was performed on CS-Al-5 V along with pure Al and ball-milled Al-5at%V alloy powder using the Rigaku SmartLab X-ray diffractometer. The samples were scanned in the 2θ range from 15° to 90° with a step size of 0.01° and a scanning rate of 1° per min. The peak shift after baseline correction was used to estimate the interplanar distance of (111) plane. The solid solubility of V in Al for CS-Al-5 V and Al-5at%V alloy powder was estimated with the help of the estimated d -spacing of (111) plane and Vegard's law [65]. A detailed procedure for estimating the solid solubility is reported in [56,66]. The average crystallite size was estimated using Scherrer's formula (Eq. 1) [11,67–72] after subtracting instrumental broadening.

$$\tau = \frac{K\lambda}{\beta \cos\theta} \quad (1)$$

Where τ is the average crystallite size, K is a dimensionless shape factor ($K=0.94$), λ is the X-ray wavelength of the source ($\lambda = 1.542 \text{ \AA}$), β is the full-width half maximum (FWHM) after subtracting instrumental broadening, and θ is the Bragg angle. The instrumental broadening was estimated using the FWHM of the corresponding (111) plane of pure Al XRD patterns.

2.2.4. Hardness test

The Vickers Hardness of the CS-Al-5 V and AA2024-T3 substrate were measured using Mitutoyo HM 112 microhardness tester. The applied load was 200 g with a dwell time of 5 s. The average Vickers hardness was estimated using ten measurements with a separating distance of at least 5 times the length of an individual indent.

2.2.5. Wear resistance test

Wear tests were performed on the CS-Al-5 V and AA2024-T3

substrate using a dry sliding ball-on-disk tribometer (T50, Nanovea, Irvine, CA). A 3 mm diameter track with a rotational speed of 100 RPM was used for the experiment. The track was rotated for 30 min while applying a normal load of 5 N using an aluminum oxide ball with a 3 mm diameter. The worn surface area and the depth profiles were estimated using optical profilometry. Eight different wear profiles of each sample were considered to estimate the average volume loss.

2.3. Electrochemical measurements

The corrosion performance of the substrate (AA2024-T3) and CS-Al-5 V samples was investigated using electrochemical tests separately. The AA2024-T3 was grounded using SiC sandpapers from P400 to P1200 mesh and ultrasonicated in ethanol for 10 min prior to the electrochemical testing. An adhesive polymer tape with an exposure area of 0.178 cm^2 was stucked to the sample to avoid crevice corrosion during the electrochemical tests. A standard three-electrode flat cell with a saturated calomel reference electrode (SCE) and Pt mesh counter electrode was used for the experiment. The test results were acquired using the VMP-300 potentiostat with the help of EC-lab software. All electrochemical tests were repeated at least three times to ensure the reproducibility of the results.

2.3.1. Potentiodynamic polarization tests

Potentiodynamic polarization (PDP) tests were conducted on AA2024-T3 and CS-Al-5 V in a non-deaerated 0.01 M NaCl aqueous solution. Open circuit potential (OCP) was measured for 30 min (OCP of HEBM Al alloys stabilizes within 30 min of immersion). Then, the anodic polarization was performed with a sweep rate of 0.167 mV s^{-1} , starting from 50 mV below OCP. The test was continued until the current density reached $200 \mu\text{A cm}^{-2}$. The potentiodynamic polarization test procedure and its parameters are described in [58,59,71–73].

2.3.2. Electrochemical impedance spectroscopy

Electrochemical impedance spectroscopy (EIS) tests were conducted on AA2024-T3 and CS-Al-5 V in a non-deaerated 0.01 M NaCl aqueous solution. OCP was measured for 30 min prior to EIS scanning. A sinusoidal wave with 10 mV amplitude with respect to OCP was passed

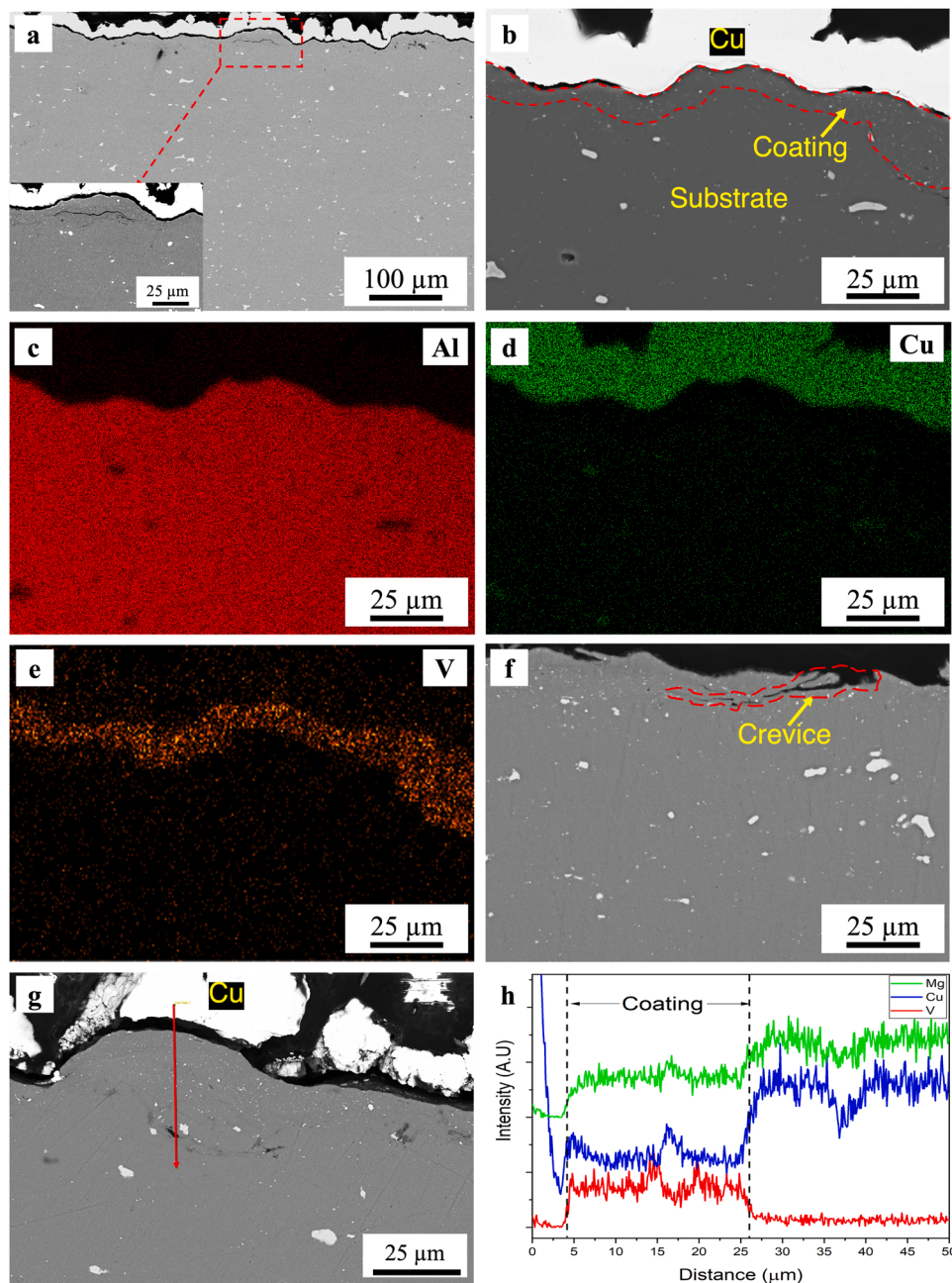


Fig. 3. Microstructural characterization of the cross-section of CS-Al-5 V coating using SEM a) Low magnification BSE image with an occasional coating debonding, b) High magnification BSE image shows the uneven coating c-e) EDXS elemental mapping of b, f) BSE image indicates an occasional crevice formation in the coating, g) BSE image reveals a region, where the EDXS line scan was performed, and h) EDXS line scan of various elements along the red arrow shown in g) (Stacked the plot to increase the visibility of the intensity of each element). (For interpretation of the references to color in this figure legend, the reader is referred to the web version of this article.)

through the sample, and the frequency of the wave varied from 100 kHz to 10 mHz. For each frequency, three readings were acquired, and ten data points were collected per frequency decade.

2.3.3. Zero resistance ammeter tests

Zero resistance ammeter tests (ZRA) were carried out using a CS-Al-5 V sample as a working electrode, while AA2024-T3 was set as a counter electrode. The exposed area for the two samples was kept the same (0.178 cm^2). OCPs of the working electrode and counter electrode were recorded for 30 min. After that, the current flow of the system was monitored for 30 min under the ZRA condition.

2.4. Immersion tests

Immersion tests for the top surface and cross-section of CS-Al-5 V were carried out. Prior to the immersion test, a cross-sectional sample was mounted on epoxy and grounded using SiC sandpapers from P400 to

P1200 mesh. The specimen was polished up to $0.05 \mu\text{m}$ surface finishing using diamond suspension and subsequently ultrasonicated in ethanol for about 10 min. The cross-sectional specimen was immersed in 0.01 M NaCl for 6 h, while the top surface of the sample was immersed in 0.01 M NaCl for 7 days. After immersion, specimens were cleaned thoroughly with de-ionized water, and SEM was performed on both samples separately. After SEM, a Cu layer was electrodeposited on the top surface immersed sample to study the cross-sectional view of the coating. The specimen was mounted on epoxy. During mounting, the cross-section of the coating was placed upward, and the same sample preparation procedure was followed prior to SEM.

3. Results and discussion

3.1. Microstructural characterization of cold sprayed coating

Fig. 1 shows a BSE image of powder particles and their size

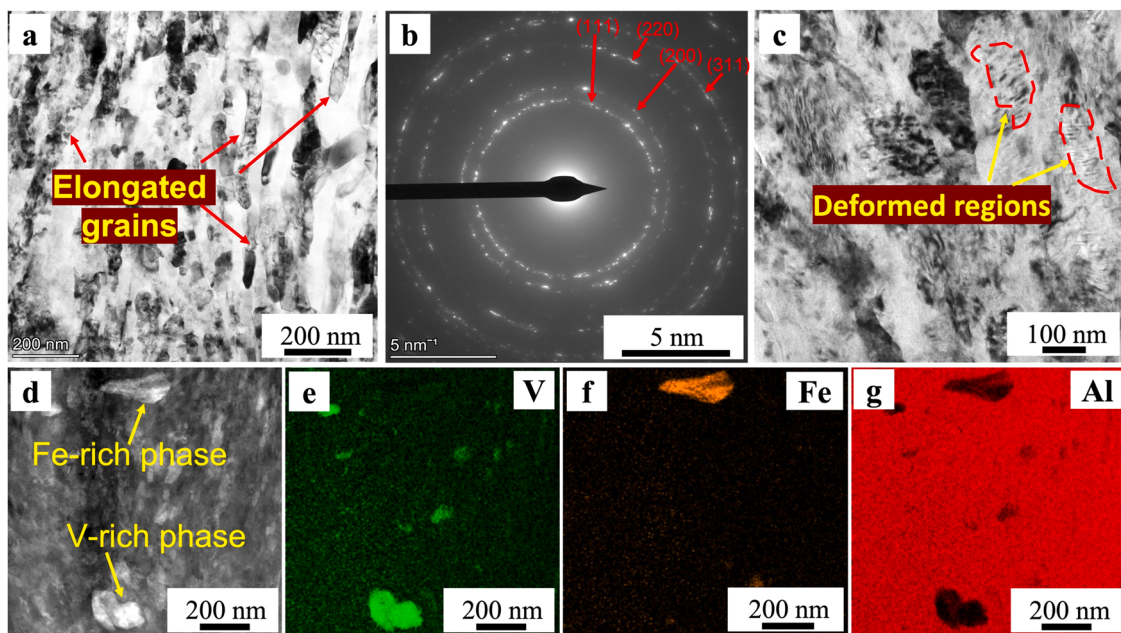


Fig. 4. BF-STEM image of CS-Al-5V showing elongated grains, b) SAED pattern exhibiting crystallite orientations of FCC Al, c) TEM image reveals several deformed regions as pointed by the yellow arrows and red dotted circle, d) HAADF-STEM image with various secondary phases in CS-Al-5 V microstructure and, e-g) EDXS elemental map, showing V-rich and Fe-rich phases. (For interpretation of the references to color in this figure legend, the reader is referred to the web version of this article.)

distribution after HEBM. Most of the particles were near-spherical shapes with a narrow particle size distribution. The average particle size, estimated using the Image J software, was $12.6 \pm 6 \mu\text{m}$. A wide range of high-energy ball-milled Al-5at%V alloy properties have been discussed in [58,60]. This alloy exhibits high thermal stability [62], high corrosion resistance [56,58,59], high strength [55,58,60], and high elastic modulus [57,64]. BSE images of the top surface of CS-Al-5 V are shown in Fig. 2a and b. Fig. 2a indicates a surface without observable holes, pores, or cracks. However, the high magnification image (Fig. 2b) exhibits interparticle boundaries. The area fraction of these interparticle boundaries, estimated using Image J software, was $\sim 6\%$. The EDXS elemental maps of Fig. 2b show the particle separation (Fig. 2c) and the presence of fine bright particles confirmed to be V-rich phases (Fig. 2d).

Cross sectional SEM images of the coating and substrate are presented in Fig. 3. Coating/substrate interface was not visible in most regions (Fig. 3a and b). However, occasional cracks and pores are observed at the coating/substrate interface (Fig. 3a). The EDXS elemental mapping was performed on the region shown in Fig. 3b and is presented in Figs. 3c-e. The observed Cu on top is electroplated copper (Fig. 3d). In Fig. 3e, V indicates the coating of Al-5at%V alloy. The coating cross-section in Fig. 3f shows an occasional crevice from the top surface towards the substrate. These crevices are rare in the coatings, albeit they could profoundly influence the mechanical and corrosion performance. The EDXS line scan on the CS-Al-5 V cross-section was performed to estimate the coating thickness. EDXS line scan presented in Fig. 3h was from the red arrow shown in Fig. 3g. The high-intensity V region in Fig. 3h revealed cold sprayed coating on the AA2024-T3 substrate. 10-line scans were performed to estimate the coating thickness, ranging from 2.5 to $21.8 \mu\text{m}$ with an average thickness of $13 \pm 7 \mu\text{m}$. This coating thickness variation could be attributed to the powder flow interruption and the nozzle's gradual clogging. Based on the cross-sectional SEM observations, the coating/ substrate interface was not distinguished from SEM, exhibiting excellent bonding.

Fig. 4 shows the STEM analysis of the cross-section of CS-Al-5 V alloy. BF-STEM image (Fig. 4a) reveals the formation of elongated grains with an average length of $100 \pm 85 \text{ nm}$ and width of $38 \pm 9 \text{ nm}$ due to severe plastic deformation. The selective area electron diffraction

(SAED) pattern shown in Fig. 4b exhibited bright rings indexed by designated grain orientations (red arrows). These bright rings indicated the formation of a nanocrystalline structure. The interplanar distance of (111) plane was extrapolated using SAED pattern and was 4.03505438 \AA . The solid solubility of V in Al was approximated considering the interplanar distance of (111) plane in pure Al 4.04958 \AA [59] and Vegard's law [65]. The estimated solid solubility of V in Al was 1.89 at\% , which is six orders of magnitude higher than that is predicted by the equilibrium phase diagram. A high magnification TEM image (Fig. 4c) exhibits several deformed regions marked by the yellow arrows. The presence of these shear regions could be attributed to the severe plastic deformation during the ball milling and cold spray process. The EDXS elemental mapping was performed on a selected region (Fig. 4d) and is presented in Figs. 4e-g. A V-rich phase was observed in several spots (Fig. 4e), which was also observed in the SEM microstructural analysis. In addition, the Fe-rich phase was observed in the microstructure (Fig. 4f) that usually comes from the abrasion of milling media during ball milling, as confirmed in our previous work [59].

The parallel beam XRD scans for CS-Al-5 V along with that for pure Al and as ball-milled Al-5at%V alloy are presented in Fig. 5. CS-Al-5 V showed only the peaks corresponding to FCC Al (Fig. 5a). The peak broadening and the decreased peak intensity were observed in CS-Al-5 V compared to pure Al, revealing the crystallite refinement. CS-Al-5 V peaks were shifted towards higher 2θ values than pure Al (Fig. 5b), indicating the reduction of lattice parameters due to the formation of Al-V solid solution. The estimated solid solubility of V in Al using XRD was 1.69 at\% , which agrees with that value estimated from TEM. It should be noted that the solid solubility of V in ball milled alloy (2.32 at\%) was higher than that in CS-Al-5 V (1.69 at\%), which is clear from the 2θ values in Fig. 5b. As determined by XRD, the average crystallite size of CS-Al-5 V was $\sim 19 \text{ nm}$, which is typical in high-energy ball-milled Al alloys [71,72,74].

3.2. Hardness and wear resistance

The hardness of the coated specimen was 314 HV , which is significantly higher than that of AA2024-T3 alloy substrate (129 HV) and ball

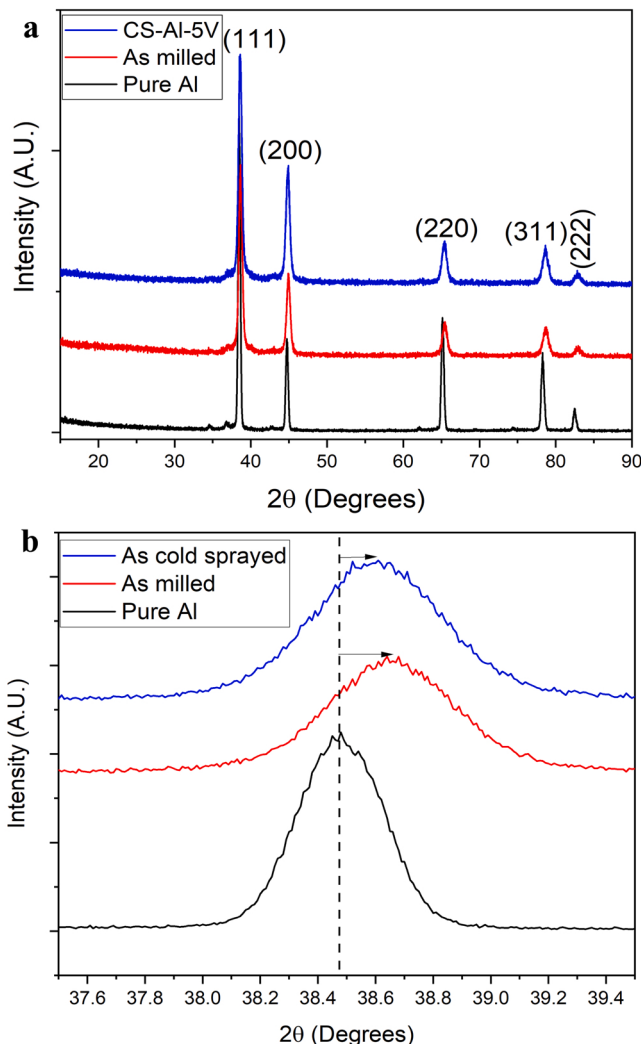


Fig. 5. XRD analysis of CS-Al-5 V compared with as milled Al-5 at%V powder and commercially available pure Al. a) Full scan, revealing only peaks corresponding to FCC Al, and b) Zoomed-in region of the (111) peak.

milled and subsequently cold compacted Al-at% 5 V alloy (245 HV). The increased hardness of the cold sprayed specimen could be mainly attributed to the nanocrystalline structure, high solid solubility of V in Al, work hardening, and precipitation hardening.

The average volume loss during the wear test of CS-Al-5 V alloy was $68 \times 10^6 \mu\text{m}^3$, whereas volume loss for substrate was $293 \times 10^6 \mu\text{m}^3$, which is almost 4 times higher than that in the coated specimen. However, a dedicated study is required to develop a mechanistic understanding of the improved wear resistance.

3.3. Corrosion behavior of cold sprayed coating

The potentiodynamic polarization curves for CS-Al-5 V and AA2024-T3 in 0.01 M NaCl are presented in Fig. 6a. The average corrosion potential (E_{corr}), corrosion current density (i_{corr}), and pitting potential (E_{pit}) were estimated considering three PDP curves and are shown in Table 1. The CS-Al-5 V exhibited high pitting potential ($-407 \text{ mV}_{\text{SCE}}$), a large and clear passive region compared to AA2024-T3. In AA2024-T3, the passive region and pitting potential were not visible as the pitting potential lie below corrosion potential [74]. Interestingly, corrosion potential for CS-Al-5 V ($-491 \text{ mV}_{\text{SCE}}$) was less noble than that of AA2024-T3 ($-465 \text{ mV}_{\text{SCE}}$), indicating the coating to be an anode in case of any galvanic interaction between substrate and coating. The average

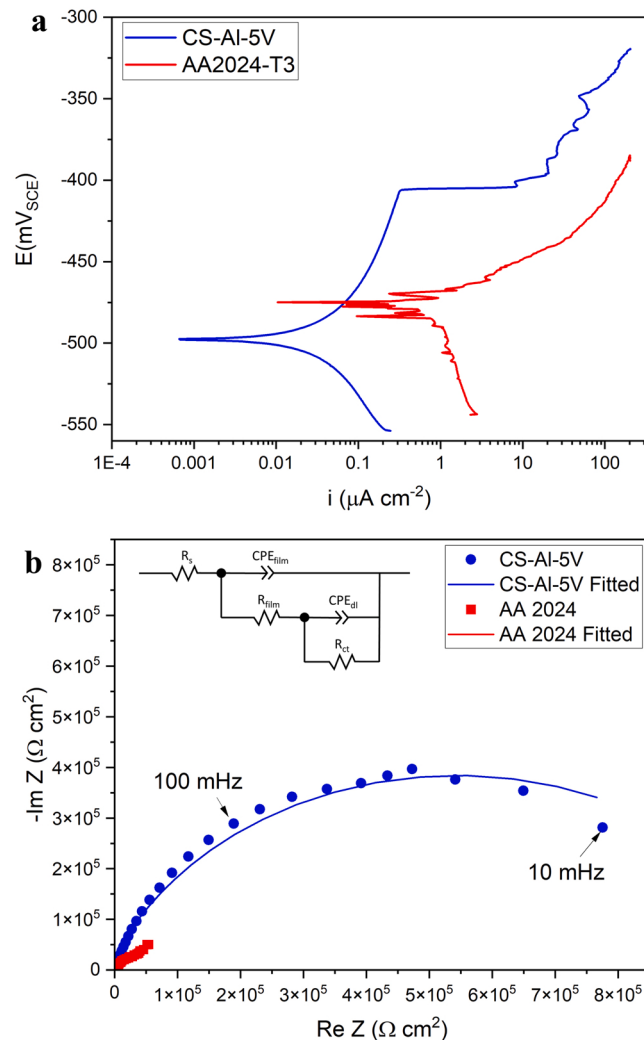


Fig. 6. Corrosion behavior of CS-Al-5 V in comparison with AA2024-T3 after 30 min of OCP stabilization in 0.01 M NaCl. a) Representative PDP curves and b) Nyquist plots with the inset image showing the equivalent circuit used for the experimental data fitting.

Table 1

The average electrochemical properties estimated using Tafel fit for CS-Al-5 V and AA2024-T3.

	$E_{\text{corr}} (\text{mV}_{\text{SCE}})$	$i_{\text{corr}} (\mu\text{A cm}^{-2})$	$E_{\text{pit}} (\text{mV}_{\text{SCE}})$
CS-Al-5V	-491 ± 29	0.02 ± 0.01	-407 ± 20
AA2024-T3	-465 ± 5	0.86 ± 0.12	-

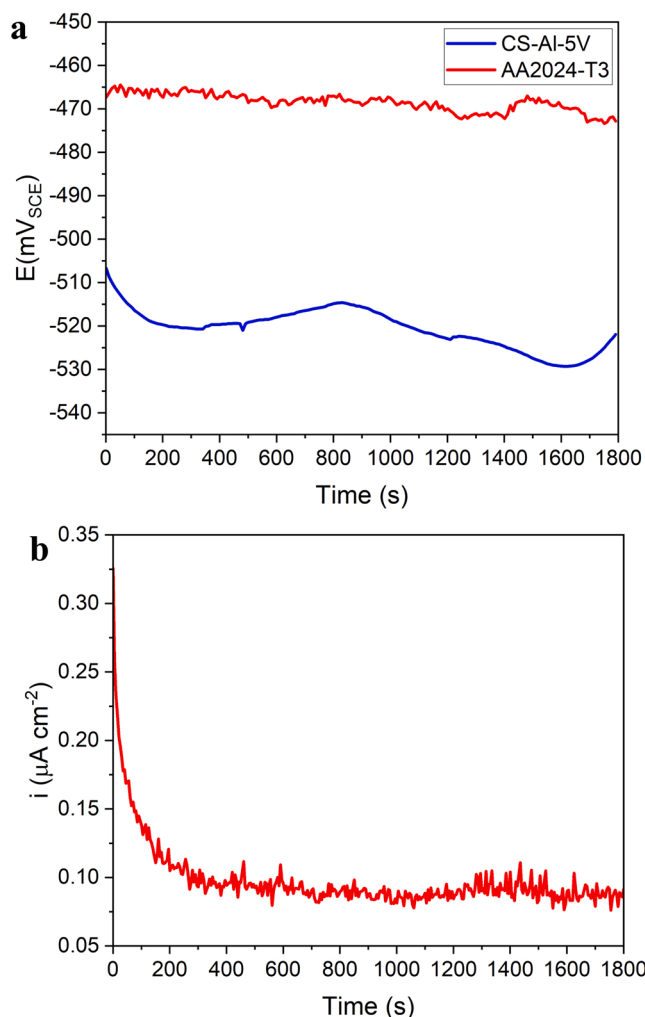
i_{corr} of AA2024-T3 and CS-Al-5 V were $0.86 \mu\text{A cm}^{-2}$ and $0.02 \mu\text{A cm}^{-2}$, respectively. The high corrosion resistance of CS-Al-5 V could be attributed to the higher solid solubility of V in Al and uniform distribution of V in the Al matrix. Detailed studies concerning the role of extended solid solubility of V and microstructure on passive film structure, passive film breakdown, pit growth, and repassivation are discussed in [59]. It should be noted that the corrosion performance of as cold sprayed sample with an uneven surface and occasional defects has been investigated. Polishing is expected to result in a further increase in corrosion resistance.

Nyquist plots for CS-Al-5 V and AA2024-T3 in 0.01 M NaCl are shown in Fig. 6b. A two-time constants equivalent circuit was used to characterize the electrochemical impedance of both samples; one is located at high frequencies, and the other is at low frequencies. These

Table 2

EIS fitting results estimated using the Zview software for CS-Al-5 V and AA2024-T3.

	R_s ($\Omega \text{ cm}^2$)	CPE_{film} ($\mu\text{F cm}^{-2}$)	CPE_{film-p}	R_{film} ($\text{k}\Omega \text{ cm}^2$)	CPE_{dl} ($\mu\text{F cm}^{-2}$)	CPE_{dl-p}	R_{ct} ($\text{k}\Omega \text{ cm}^2$)	Chi-Squared ($\times 10^{-2}$)
CS-Al-5 V	294	3.5	0.83	921	3.6	0.81	1026	0.4
AA2024-T3	251	4.2	0.83	73	15.1	0.85	166	0.8

**Fig. 7.** ZRA tests between CS-Al-5 V (working electrode) and AA2024-T3 (counter electrode), showing a) OCP relaxation and b) The current flow from the working electrode to the counter electrode over time.

two-time constants are associated with passivity and localized corrosion [75]. The EIS data for both CS-Al-5 V and AA2024-T3 were fitted using Zview software with the help of the equivalent circuit shown in the inset of Fig. 6b, where R_s is the solution resistance, CPE_{film} and R_{film} correspond to the surface film's constant phase element and the resistance, respectively. CPE_{dl} and R_{ct} indicate the double layer constant phase element and charge transfer resistance, respectively. A constant phase element (CPE) indicated the frequency-dependent non-ideal capacitive behavior. The highest total impedance ($|Z|$) of CS-Al-5 V was $659 \text{ k}\Omega \text{ cm}^2$, 50 times higher than that in AA2024-T3, revealing the remarkable improvement in corrosion resistance due to the cold sprayed coating. In addition, both passive film resistance (R_{film}) and charge transfer resistance (R_{ct}) of CS-Al-5 V were significantly higher than that in AA2024-T3 (Table 2). The effect of V and HEBM could be ascribed to the enhanced passive film and charge transfer resistance in CS-Al-5 V [59,71]. The constant phase element of the double-layer formed on

AA2024-T3 substrate was $15 \mu\text{F cm}^{-2}$, which is 4 times higher than that of CS-Al-5 V, showing a lower susceptibility to localized corrosion in the CS-Al-5 V than that of the AA2024-T3 substrate. This could be attributed to the inhibitive nature of V in localized corrosion sites, as discussed in [58,59,71]. In addition, the film constant phase element of CS-Al-5 V was slightly lower than that of the substrate alloy. This indicates slightly higher passive film stability in CS-Al-5 V, possibly due to lower conductivity of the passive than in the AA2024-T3 substrate. Therefore, the chloride ion penetration through the passive film in CS-Al-5 V alloy could be restricted compared to that in AA2024-T3.

The zero-resistance ammeter (ZRA) test was performed to understand the galvanic coupling between CS-Al-5 V and AA2024-T3. OCP of CS-Al-5 V coating was $-520 \text{ mV}_{\text{SCE}}$, which is 60 mV lower than that of AA2024-T3 (Fig. 6a and Fig. 7a). This exhibits that the CS-Al-5 V coating is anodic to the AA2024-T3 substrate, which can protect the substrate in case of coating breakdown or defects. In addition, the positive current pulse was observed during the ZRA scanning (Fig. 7b) and converged to $0.1 \mu\text{A cm}^{-2}$ over time, which indicates reduced galvanic interaction between the coating and the substrate as compared to that in the reported literature [76].

3.4. Post corrosion characterization of the coating

The SEM analysis of the top of CS-Al-5 V coating after immersion in 0.01 M NaCl for 7 days is presented in Fig. 8. A BSE image (Fig. 8a) exhibits the presence of corrosion products on the coating surface. The high magnification BSE image (Fig. 8b) reveals cracks on the coating surface, where localized corrosion products were observed.

A coating cross-section was scanned at several regions and is presented in Fig. 8c and d. Fig. 8c exhibits a coating region where the substrate is protected by coating without localized corrosion. The elemental O was not detected (EDXS analysis Fig. 8c) on top of the substrate, revealing the absence of significant corrosion at the coating/substrate interface. Fig. 8d shows the localized corrosion at the coating and substrate interface. The coating was discontinued in the region where the localized corrosion was noticed. The absence of the coating or the presence of a coating defect, such as a crevice (Fig. 3f), could expose the substrate to the electrolyte, which can initiate localized corrosion. In addition, a Cu-rich region was detected inside the pit, confirming the severe influence of the cathodic Cu particles on localized corrosion initiation. The accumulation of corrosion products at the coating/substrate interface could lead to the generation of stresses on the coating near localized corrosion points. These stresses could have resulted in cracks formation and releasing the corrosion products to the top of the coating via forming cracks, as observed in Fig. 8b.

Fig. 9 shows SEM images of CS-Al-5 V coating cross-section after 6 h of immersion in 0.01 M NaCl . The BSE image of the cross-section (Fig. 9a) revealed the localized corrosion initiation at Cu-rich sites, which is a well-known phenomenon for AA2024-T3 [77,78]. A zoomed-in region selected from Fig. 9a is presented in Fig. 9b, along with the EDXS elemental mapping. The absence of corrosion at the interface between coating and substrate was observed (Fig. 9b). In EDXS elemental mapping, V and O indicate the coating of Al-5at%V alloy and corrosion products, respectively. The elemental oxygen was not detected along with the interface of coating/substrate, exhibiting the least corrosion between the coating and substrate. This shows the excellent galvanic compatibility between the coating and the substrate, compared with reported coatings for Al alloys [79]. However, a layer of corrosion

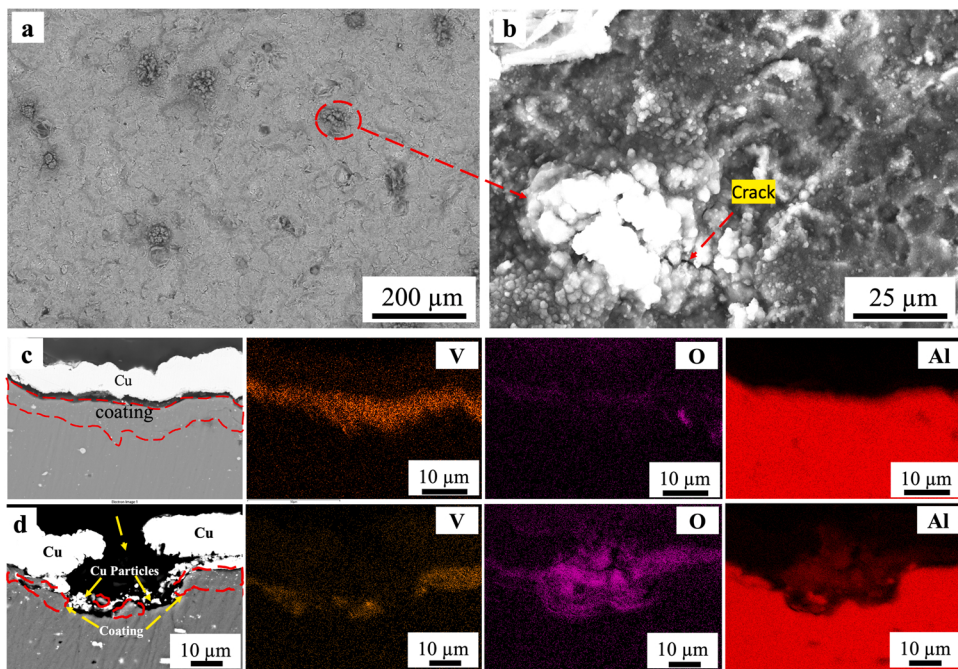


Fig. 8. Corrosion characterization using SEM. The top surface was exposed to 0.01 M NaCl for 7 days. a) A BSE image of the top surface of the coating with the localized corrosion initiation, b) A selected localized corrosion point from Fig. 8a, showing the formation of cracks around the corrosion products, c) A coating without observable defects, leading to the protection of the substrate. The EDXS analysis shows the elemental distribution around the uncorroded coating, d) Localized corrosion at the interface between the coating and the substrate. The EDXS elemental map reveals the presence of Cu-rich particles caused corrosion initiation.

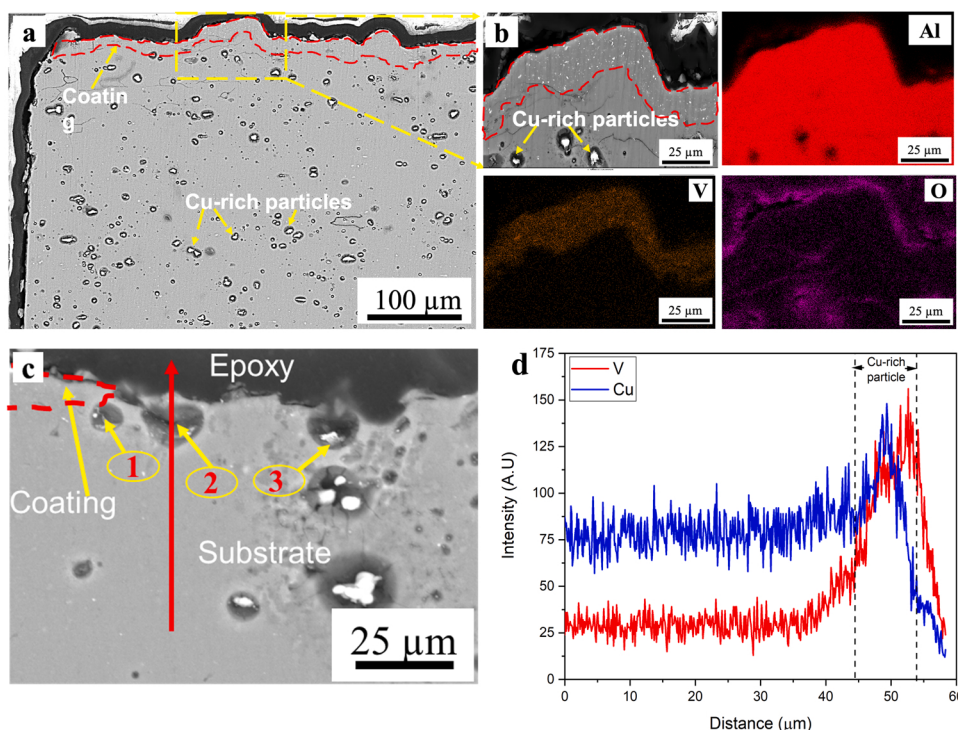


Fig. 9. SEM analysis of coating cross-section after immersing in 0.01 M NaCl for 6 h. a) BSE image of the cross-section, showing the localized corrosion initiation at Cu-rich sites b) A selected zoomed-in region from Fig. 9a. The EDXS maps of Fig. 9b indicate the absence of corrosion at the interface between coating and substrate, c) high magnification BSE image near the coating/substrate interface and d) EDXS line scan of elemental Cu and V along the red arrow shown in (c). (For interpretation of the references to color in this figure legend, the reader is referred to the web version of this article.)

products was detected (Fig. 9 EDXS oxygen elemental mapping) above the coating layer due to the crevice corrosion at the separated interface between the coating and the mounted epoxy. Fig. 9c shows a selected zoomed-in region near the coating/substrate interface, where the copper-rich particles are present in the substrate. Corrosion was observed around the copper-rich particles due to their cathodic nature. EDXS lines scans (red arrow in Fig. 9c) were performed through the particles named as 1, 2, and 3 in Fig. 9c, confirming all three particles to be rich in Cu. The EDXS line scan through particle 2 is presented in Fig. 9d. Interestingly, V enrichment was observed around the Cu-rich

particles (Fig. 9d), which could be because of the release of the V from corrosion of coating and subsequent deposition on the cathodic sites. This phenomenon has been shown for Al-V alloys through TEM analysis of pits and regions near pits in ball-milled Al-V alloys [58,59]. It was postulated that the V deposition on cathodic sites could decrease their efficiency in sustaining cathodic current and retard the pitting corrosion. However, this proposed phenomenon of V release and subsequent deposition in cold spray coatings needs to be investigated in future studies.

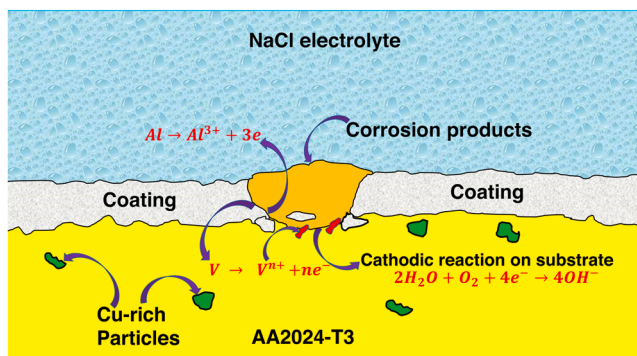


Fig. 10. Schematic diagram shows the proposed corrosion mechanisms of the alloy with corrosion initiation within the coating and the interface between the coating and the substrate. V deposition occurs at the substrate in case of coating breakdown.

3.5. General discussion

The plastic deformation and ductility of the feedstock powder play a crucial role in forming strong metallic bonds between substrate and coating, determining the cold spray coating characteristics [42,80]. Combining appropriate cold spray processing conditions and Al-5at%V feedstock powder is expected to result in a dense and fully compacted coating along with interparticle boundaries. The cold spray parameters used herein were similar to that used for pure Al. Furthermore, optimization of processing parameters is expected to result in further improvement in coating characteristics. Feedstock alloy powder exhibited a nanocrystalline structure and high solid solubility of V in Al which are attributed to the high hardness of the feedstock alloy powder [58,60]. However, further increment of the hardness of CS-Al-5 V could be attributed to work hardening by the cold spray. In addition, precipitation hardening is also possible in Al-5at%V alloy, as reported in the literature [58].

The corrosion resistance of feedstock Al-5at%V alloy was studied after cold compaction of ball milled powder and reported to be significantly higher than that of AA2024-T3 substrate [56,58]. Furthermore, it has been reported that the formation of high solid solubility of V in Al and improved passive film stability due to the effect of high energy ball milling and the addition of V caused enhanced corrosion resistance in Al-V alloys [56,59]. Interestingly, the solid solubility of V in cold spray coating was in the same order of magnitude as in the feedstock alloy powder, indicating the retention of initial solid solubility even after cold spray. Therefore, it is clear that the corrosion resistance enhancement in CS-Al-5 V, as shown by PDP and EIS tests, is mainly attributed to the corrosion resistance of feedstock Al-5at%V powder.

The schematic representation of coating, substrate and electrolyte in Fig. 10 elucidates localized corrosion initiation at the interface between coating and substrate. The occasional discontinuity, such as a crevice formation during cold spray (Fig. 3f), facilitates electrolyte penetration toward the coating-substrate interface. Once the electrolyte has reached the coating/substrate interface, localized corrosion is favored due to the galvanic interaction between coating and substrate. Furthermore, the coating acts as an anode to the substrate, and the corrosion of the coating can be hypothesized to release V and Al ions. The released V ions could inhibit the corrosion at the coating/substrate interface. The inhibition mechanism could be similar to that reported for vanadates and other corrosion inhibitors [54,59,81,82]. This hypothesis of vanadium release on repassivation for the cold-sprayed alloys needs to be validated in future studies. Nonetheless, the deposition of V on cathodic Fe and C-rich particles in Al-V alloys resulting in high corrosion resistance has been shown elegantly by Christudasjustus et al. [58] and Witharamage et al. [59] by analyzing the pits using scanning transmission electron microscopy.

4. Conclusions

Al-5at%V alloy powder with high solid solubility of V and nanocrystalline structure was produced via high-energy ball milling. This ball-milled alloy powder was successfully deposited on the AA2024-T3 substrate using the cold spray, resulting in a dense coating, and the following are the conclusions:

- Cold sprayed coating of Al-5at%V alloy revealed a nanocrystalline structure along with six orders of magnitude higher solid solubility of V in Al than that predicted by the phase diagram. It should be noted that the solid solubility of V in high-energy ball milled alloy was 2.32 at% which decreased to 1.7 at% V after cold spray.
- The wear resistance of the cold sprayed alloy was 4.3 times higher than that of AA2024-T3 substrate. In addition, the hardness after cold spraying Al-5at%V was 2.4 times higher than that of the substrate and 1.3 times higher than that of the ball-milled and subsequently cold-compacted Al-5at%V alloy. High hardness and wear resistance after cold spray could be attributed to grain refinement, work hardening, solid solution strengthening, and precipitation strengthening.
- The cold sprayed alloy exhibited low corrosion current density (43 times lower than that of the substrate) and a clear passive window with a high pitting potential ($-407 \text{ mV}_{\text{SCE}}$). This high corrosion resistance has been attributed to the nanocrystalline structure and high solid solubility of V in Al.
- The galvanic compatibility between the cold sprayed coating, and the substrate was excellent. Zero resistance ammeter tests showed that the coating acts as a sacrificial anode to the substrate, indicating its ability to protect the substrate from corrosion in the event of coating breakdown.
- Cold sprayed coatings of ball-milled alloys could be applied to a wide range of Al alloys, which can expand the application of high-strength Al alloys in harsh environments. Moreover, the composition and microstructure of the coatings can be varied according to the electrochemical properties of the substrate.

CRediT authorship contribution statement

C.S. Witharamage: Conceptualization, Methodology, Investigation, Formal analysis, Data curation, Writing – original draft, Writing – review & editing. **M.A. Alrizqi:** Methodology, Investigation, Formal analysis. **J. Chirstudasjustus:** Investigation, Formal analysis. **Ahmed A. Darwish:** Investigation, Formal analysis. **A. Troy:** Investigation (wear tests). **A. Nieto:** Methodology, Investigation, Formal analysis, Writing – review & editing. **R.K. Gupta:** Conceptualization, Methodology, Writing – original draft, Writing – review & editing, Supervision, Project administration, Funding acquisition.

Declaration of Competing Interest

The authors declare that they have no known competing financial interests or personal relationships that could have appeared to influence the work reported in this paper.

Data availability

Data will be made available on request.

Acknowledgements

This work was supported by the National Science Foundation (NSF-CMMI 2131440) under the direction of Dr. Alexis Lewis. In addition, the authors would like to acknowledge the Analytical Instrument Facility (AIF) at North Carolina State University for facilitating the SEM and XRD tests.

References

- [1] B. Minhas, S. Dino, L. Huang, D. Wu, Active corrosion protection by epoxy coating on Li₂CO₃-pretreated anodized aluminum alloy 2024-T3, *Front Mater.* 8 (2022) 589, <https://doi.org/10.3389/FMATS.2021.804328/BIBTEX>.
- [2] J.V. Nardelli, D.V. Snihirova, C.S. Fugivara, M.F. Montemor, E.R.P. Pinto, Y. Messadecq, A.V. Benedetti, Localised corrosion assessment of crambe-oil-based polyurethane coatings applied on the ASTM 1200 aluminum alloy, *Corros. Sci.* 111 (2016) 422–435, <https://doi.org/10.1016/J.CORSCI.2016.05.034>.
- [3] P. Visser, Y. Liu, X. Zhou, T. Hashimoto, G.E. Thompson, S.B. Lyon, L.G.J. Van Der Ven, A.J.M.C. Mol, H.A. Terryn, The corrosion protection of AA2024-T3 aluminium alloy by leaching of lithium-containing salts from organic coatings, *Faraday Discuss.* 180 (2015) 511–526, <https://doi.org/10.1039/C4FD00237G>.
- [4] S. Roshan, A.A. Sarabi, Improved performance of Ti-based conversion coating in the presence of Ce/Co ions: surface characterization, electrochemical and adhesion study, *Surf. Coat. Technol.* 410 (2021), 126931, <https://doi.org/10.1016/J.SURFCOAT.2021.126931>.
- [5] W. Zhu, W. Li, S. Mu, N. Fu, Z. Liao, Comparative study on Ti/Zr/V and chromate conversion treated aluminum alloys: anti-corrosion performance and epoxy coating adhesion properties, *Appl. Surf. Sci.* 405 (2017) 157–168, <https://doi.org/10.1016/JAPSUSC.2017.02.046>.
- [6] S. Chen, S. Zhang, X. Ren, S. Xu, L. Yin, Cerium-based chemical conversion coating on aluminum alloy to inhibits corrosion in chloride solution, *Electrochim. Org.* 10 (2015) 9073–9088.
- [7] B. Valdez, S. Kiyota, M. Stoytcheva, R. Zlatev, J.M. Bastidas, Cerium-based conversion coatings to improve the corrosion resistance of aluminium alloy 6061-T6, *Corros. Sci.* 87 (2014) 141–149, <https://doi.org/10.1016/J.CORSCI.2014.06.023>.
- [8] I. Milosev, G.S. Frankel, Review—conversion coatings based on zirconium and/or titanium, *J. Electrochem Soc.* 165 (2018) C127–C144, <https://doi.org/10.1149/2.0371803JES/XML>.
- [9] M. Becker, Chromate-free chemical conversion coatings for aluminum alloys, *Corros. Rev.* 37 (2019) 321–342, https://doi.org/10.1515/CORREV-2019-0032/ASSET/GRAFIC/J.CORREV-2019-0032 FIG_002.JPG.
- [10] A.E. Hughes, R.J. Taylor, B.R.W. Hinton, Chromate conversion coatings on 2024 Al alloy, *Surf. Interface Anal.* 25 (1997) 223–234, [https://doi.org/10.1002/\(SICI\)1096-9918\(199704\)25:4<223::AID-SI1>3.0.CO;2-1](https://doi.org/10.1002/(SICI)1096-9918(199704)25:4<223::AID-SI1>3.0.CO;2-1).
- [11] A.S. Nguyen, M. Musiani, M.E. Orazem, N. Pébère, B. Tribollet, V. Vivier, Impedance study of the influence of chromates on the properties of waterborne coatings deposited on 2024 aluminium alloy, *Corros. Sci.* 109 (2016) 174–181, <https://doi.org/10.1016/j.jcrosci.2016.03.030>.
- [12] G.S. Frankel, R.L. McCreery, Inhibition of Al alloy corrosion by chromates, *Electrochim. Soc. Interface* 10 (2001) 34–38, <https://doi.org/10.1149/2.F06014IF/XML>.
- [13] T.A. Markley, J.I. Mardel, A.E. Hughes, B.R.W. Hinton, A.M. Glenn, M. Forsyth, Chromate replacement in coatings for corrosion protection of aerospace aluminium alloys, *Mater. Corros.* 62 (2011) 836–840, <https://doi.org/10.1002/MACO.200905597>.
- [14] R.L. Twite, G.P. Bierwagen, Review of alternatives to chromate for corrosion protection of aluminum aerospace alloys, *Prog. Org. Coat.* 33 (1998) 91–100, [https://doi.org/10.1016/S0300-9440\(98\)00015-0](https://doi.org/10.1016/S0300-9440(98)00015-0).
- [15] O. Gharbi, S. Thomas, C. Smith, N. Birbilis, Chromate replacement: what does the future hold, *Npj Mater. Degrad.* 2 (2018) 1–8, <https://doi.org/10.1038/s41529-018-0034-5>.
- [16] R. Riastuti, S.T. Siallagan, Z. Rahmat, B.A.H. Bancin, The study of mechanical properties and corrosion resistance of molybdenum coating and aluminum coating using thermal spray method on stainless steel 316L, *IOP Conf. Ser. Mater. Sci. Eng.* 420 (2018), 012058, <https://doi.org/10.1088/1757-899X/420/1/012058>.
- [17] G.C. Saha, T.I. Khan, G.A. Zhang, Erosion-corrosion resistance of microcrystalline and near-nanocrystalline WC-17Co high velocity oxy-fuel thermal spray coatings, *Corros. Sci.* 53 (2011) 2106–2114, <https://doi.org/10.1016/J.CORSCI.2011.02.028>.
- [18] M. Carboneras, M.D. López, P. Rodrigo, M. Campo, B. Torres, E. Otero, J. Rams, Corrosion behaviour of thermally sprayed Al and Al/SiC composite coatings on ZE41 magnesium alloy in chloride medium, *Corros. Sci.* 52 (2010) 761–768, <https://doi.org/10.1016/J.CORSCI.2009.10.040>.
- [19] L. Sun, G. Yuan, L. Gao, J. Yang, M. Chhowalla, M.H. Gharahcheshmeh, K. Gleason, Y.S. Choi, B.H. Hong, Z. Liu, Chemical vapour deposition, *Nat. Rev. Methods Prim.* 1 (1) (2021) 5–20, <https://doi.org/10.1038/s43586-020-00005-y>.
- [20] V.K. Champagne, The Cold Spray Materials Deposition Process: Fundamentals and Applications, Elsevier Ltd, 2007, <https://doi.org/10.1533/9781845693787>.
- [21] A. Alkhimov, V. Kosarev, A.P.-D.A. Nauk, U, A method of cold gas-dynamic spraying, *Sov. Phys. Dokl.* 35 (1990) 1047–1049. (<http://www.mathnet.ru/eng/dan49027>).
- [22] A.P. Alkhimov, V.F. Kosarev, A.N. Papyrin, Gas-dynamic spraying. An experimental study of the spraying process, *J. Appl. Mech. Tech. Phys.* 39 (1998) 318–323, <https://doi.org/10.1007/BF02468100>.
- [23] P. Poza, M.Á. Garrido-Maneiro, Cold-sprayed coatings: microstructure, mechanical properties, and wear behaviour, *Prog. Mater. Sci.* 123 (2022), 100839, <https://doi.org/10.1016/J.PMATSCI.2021.100839>.
- [24] M. Diab, X. Pang, H. Jahed, The effect of pure aluminum cold spray coating on corrosion and corrosion fatigue of magnesium (3% Al-1% Zn) extrusion, *Surf. Coat. Technol.* 309 (2017) 423–435, <https://doi.org/10.1016/J.SURFCOAT.2016.11.014>.
- [25] K. Balani, T. Laha, A. Agarwal, J. Karthikeyan, N. Munroe, Effect of carrier gases on microstructural and electrochemical behavior of cold-sprayed 1100 aluminum coating, *Surf. Coat. Technol.* 195 (2005) 272–279, <https://doi.org/10.1016/J.SURFCOAT.2004.06.028>.
- [26] A.C. Hall, L.N. Brewer, T.J. Roemer, Preparation of aluminum coatings containing homogenous nanocrystalline microstructures using the cold spray process, *J. Therm. Spray. Technol.* 17 (2008) 352–359, <https://doi.org/10.1007/S11666-008-9180-6>.
- [27] M.R. Rokni, C.A. Widener, V.K. Champagne, G.A. Crawford, Microstructure and mechanical properties of cold sprayed 7075 deposition during non-isothermal annealing, *Surf. Coat. Technol.* 276 (2015) 305–315, <https://doi.org/10.1016/J.SURFCOAT.2015.07.016>.
- [28] H. Zhang, C. Zhao, B. Cui, X. Yan, C. Dou, T. Shao, R. Pan, The corrosion behavior of cold spray coating on 2219 aluminium alloy joints prepared by friction stir welding, *J. Phys. Conf. Ser.* 1063 (2018), 012070, <https://doi.org/10.1088/1742-6596/1063/1/012070>.
- [29] F.F. Lu, K. Ma, C.X. Li, M. Yasir, X.T. Luo, C. Jiu Li, Enhanced corrosion resistance of cold-sprayed and shot-peened aluminum coatings on LA43M magnesium alloy, *Surf. Coat. Technol.* 394 (2020), 125865, <https://doi.org/10.1016/J.SURFCOAT.2020.125865>.
- [30] E. Sansoucy, G.E. Kim, A.L. Moran, B. Jodoin, Mechanical characteristics of Al-Co-Ce coatings produced by the cold spray process, *J. Therm. Spray. Technol.* 16 (2007) 651–660, <https://doi.org/10.1007/S11666-007-9099-3>.
- [31] L. Zhang, Y. Zhang, H. Wu, S. Yang, X. Jie, Structure and corrosion behavior of cold-sprayed Cu/Ni composite coating post-treated by ultrasonic shot peening, *SN Appl. Sci.* 2 (2020) 1–14, <https://doi.org/10.1007/S42452-020-1997-8/FIGURES/10>.
- [32] B. Guerreiro, P. Vo, D. Poirier, J.G. Legoux, X. Zhang, J.D. Giallonardo, Factors affecting the ductility of cold-sprayed copper coatings, *J. Therm. Spray. Technol.* 29 (2020) 630–641, <https://doi.org/10.1007/S11666-020-00993-Z/FIGURES/12>.
- [33] V.K. Champagne, D. Helfritch, P. Leyman, S. Grendahl, B. Klotz, Interface material mixing formed by the deposition of copper on aluminum by means of the cold spray process, *J. Therm. Spray. Technol.* 14 (2005) 330–334, <https://doi.org/10.1361/105996305X59332>.
- [34] P. Cavaliere, A. Silvello, N. Cinca, H. Canales, S. Dosta, I. Garcia Cano, J. M. Guilemany, Microstructural and fatigue behavior of cold sprayed Ni-based superalloys coatings, *Surf. Coat. Technol.* 324 (2017) 390–402, <https://doi.org/10.1016/J.SURFCOAT.2017.06.006>.
- [35] A. Silvello, P. Cavaliere, A. Rizzo, D. Valerini, S. Dosta Parras, I.G. Cano, Fatigue bending behavior of cold-sprayed nickel-based superalloy coatings, *J. Therm. Spray. Technol.* 28 (2019) 930–938, <https://doi.org/10.1007/s11666-019-00865-1>.
- [36] F. Rubino, V. Paradiso, A. Astarita, P. Carbone, A. Squillace, Advances in titanium on aluminium alloys cold spray coatings, *Cold Spray. Coat. Recent Trends Future Perspect.* (2017) 225–249, <https://doi.org/10.1007/978-3-319-67183-3-7>.
- [37] M. Daroonparvar, M.U.F. Khan, Y. Saadeh, C.M. Kay, A.K. Kasar, P. Kumar, L. Esteves, M. Misra, P. Menezes, P.R. Kalvala, H.R. Bakhsheshi-Rad, R.K. Gupta, Modification of surface hardness, wear resistance and corrosion resistance of cold spray Al coated AZ31B Mg alloy using cold spray double layered Ta/Ti coating in 3.5 wt% NaCl solution, *Corros. Sci.* 176 (2020), 109029, <https://doi.org/10.1016/J.CORSCI.2020.109029>.
- [38] C.J. Akisín, F. Venturi, M. Bai, C.J. Bennett, T. Hussain, Microstructure, mechanical and wear resistance properties of low-pressure cold-sprayed Al-7 Mg/Al2O3 and Al-10 Mg/Al2O3 composite coatings, *Emergent Mater.* 4 (2021) 1569–1581, <https://doi.org/10.1007/S42247-021-00293-4/FIGURES/10>.
- [39] A.G. Gavras, D.A. Lados, V.K. Champagne, R.J. Warren, D. Singh, Small fatigue crack growth mechanisms and interfacial stability in cold-spray 6061 aluminum alloys and coatings, *Met. Mater. Trans. A Phys. Met. Mater. Sci.* 49 (2018) 6509–6520, <https://doi.org/10.1007/S11661-018-4929-0/FIGURES/11>.
- [40] A.G. Gavras, D.A. Lados, V.K. Champagne, R.J. Warren, Effects of processing on microstructure evolution and fatigue crack growth mechanisms in cold-spray 6061 aluminum alloy, *Int. J. Fatigue* 110 (2018) 49–62, <https://doi.org/10.1016/J.IJFATIGUE.2018.01.006>.
- [41] A. Moridi, S.M. Hassani-Gangaraj, M. Guagliano, S. Vezzu, Effect of cold spray deposition of similar material on fatigue behavior of Al 6082 alloy, *Conf. Proc. Soc. Exp. Mech. Ser.* 7 (2014) 51–57, https://doi.org/10.1007/978-3-319-00765-6_8/FIGURES/00086.
- [42] M.R. Rokni, S.R. Nutt, C.A. Widener, V.K. Champagne, R.H. Hrabe, Review of relationship between particle deformation, coating microstructure, and properties in high-pressure cold spray, *J. Therm. Spray. Technol.* 26 (2017) 1308–1355, <https://doi.org/10.1007/S11666-017-0575-0>.
- [43] F.S. da Silva, N. Cinca, S. Dosta, I.G. Cano, J.M. Guilemany, A.V. Benedetti, Cold gas spray coatings: basic principles corrosion protection and applications, *Eclética Quím.* 42 (2017) 09–32, <https://doi.org/10.26850/1678-4618EQJ.V42.1.2017.P09-32>.
- [44] P. Cavaliere, A. Silvello, Crack repair in aerospace aluminum alloy panels by cold spray, *J. Therm. Spray. Technol.* 26 (2017) 661–670, <https://doi.org/10.1007/S11666-017-0534-9/FIGURES/13>.
- [45] S. Yin, P. Cavaliere, B. Aldwell, R. Jenkins, H. Liao, W. Li, R. Lupoi, Cold spray additive manufacturing and repair: fundamentals and applications, *Addit. Manuf.* 21 (2018) 628–650, <https://doi.org/10.1016/J.ADDMA.2018.04.017>.
- [46] V. Champagne, D. Helfritch, Critical assessment 11: structural repairs by cold spray, *Mater. Sci. Technol.* 31 (2015) 627–634, <https://doi.org/10.1179/1743284714Y.0000000223>.
- [47] Q. Blochet, F. Delloro, F. N'Guyen, D. Jeulin, F. Borit, M. Jeandin, Effect of the cold-sprayed aluminum coating-substrate interface morphology on bond strength for aircraft repair application, *J. Therm. Spray. Technol.* 26 (2017) 671–686, <https://doi.org/10.1007/S11666-017-0548-3/TABLES/7>.

- [48] V.K. Champagne, The repair of magnesium rotorcraft components by cold spray, *J. Fail. Anal. Prev.* 8 (2008) 164–175, <https://doi.org/10.1007/S11668-008-9116-Y/FIGURES/6>.
- [49] V. Champagne, M. Trexler, D. Helfritch, Y. Sohn, G. Kim, Cold spray consolidation of nanostructured AA5083 aluminum powder, *World J. Eng.* (2010).
- [50] X. Xie, B. Hosni, C. Chen, H. Wu, Y. Li, Z. Chen, C. Verdy, O.E.I. Kedim, Q. Zhong, A. Addad, C. Coddet, G. Ji, H. Liao, Corrosion behavior of cold sprayed 7075Al composite coating reinforced with TiB₂ nanoparticles, *Surf. Coat. Technol.* 404 (2020), 126460, <https://doi.org/10.1016/J.SURFCOAT.2020.126460>.
- [51] F.S. da Silva, N. Cinca, S. Dosta, I.G. Cano, M. Couto, J.M. Guilemany, A.V. Benedetti, Corrosion behavior of WC-Co coatings deposited by cold gas spray onto AA 7075-T6, *Corros. Sci.* 136 (2018) 231–243, <https://doi.org/10.1016/J.CORSCI.2018.03.010>.
- [52] F.S. da Silva, N. Cinca, S. Dosta, I.G. Cano, J.M. Guilemany, A.V. Benedetti, Effect of the outer layer of Al coatings deposited by cold gas spray on the microstructure, mechanical properties and corrosion resistance of the AA 7075-T6 aluminum alloy, *J. Therm. Spray. Technol.* 29 (2020) 1040–1053, <https://doi.org/10.1007/s11666-020-01023-8>.
- [53] W.Y. Li, R.R. Jiang, C.J. Huang, Z.H. Zhang, Y. Feng, Effect of cold sprayed Al coating on mechanical property and corrosion behavior of friction stir welded AA2024-T351 joint, *Mater. Des.* 65 (2015) 757–761, <https://doi.org/10.1016/j.matdes.2014.10.007>.
- [54] J. Esquivel, R.K. Gupta, Review—corrosion-resistant metastable Al alloys: an overview of corrosion mechanisms, *J. Electrochem Soc.* 167 (2020), 081504, <https://doi.org/10.1149/1945-7111/AB8A97>.
- [55] J. Esquivel, R.K. Gupta, Influence of the V content on microstructure and hardness of high-energy ball milled nanocrystalline Al-V alloys, *J. Alloy. Compd.* 760 (2018) 63–70, <https://doi.org/10.1016/J.JALLCOM.2018.05.132>.
- [56] J. Esquivel, H.A. Murdoch, K.A. Darling, Excellent corrosion resistance and hardness in Al alloys by extended solid solubility and nanocrystalline structure, *Mater. Res. Lett.* 6 (2018) 79–83, <https://doi.org/10.1080/21663831.2017.1396262>.
- [57] J. Christudasjustus, C.S. Witharamage, G. Walunj, T. Borkar, R.K. Gupta, The influence of spark plasma sintering temperatures on the microstructure, hardness, and elastic modulus of the nanocrystalline Al-xV alloys produced by high-energy ball milling, *J. Mater. Sci. Technol.* 122 (2022) 68–76, <https://doi.org/10.1016/J.JMST.2022.02.008>.
- [58] J. Christudasjustus, M.R. Felde, C.S. Witharamage, J. Esquivel, A.A. Darwish, C. Winkler, R.K. Gupta, Age-hardening behavior, corrosion mechanisms, and passive film of nanocrystalline Al-V alloy exhibiting supersaturated solid solution, *J. Mater. Sci. Technol.*, (2022).
- [59] C.S. Witharamage, J. Christudasjustus, J. Smith, W. Gao, R.K. Gupta, Corrosion behavior of an in-situ consolidated nanocrystalline Al-V alloys, *Npj Mater. Degrad.* 6 (2022).
- [60] C.S. Witharamage, J. Christudasjustus, R.K. Gupta, The effect of milling time and speed on solid solubility, grain size, and hardness of Al-V alloys, *J. Mater. Eng. Perform.* 30 (2021) 3144–3158, <https://doi.org/10.1007/S11665-021-05663-X/FIGURES/21>.
- [61] C.S. Witharamage, The influence of ball milling time on solid solubility, Grain Size and Hardness of Al-V Alloys, The University of Akron, 2020.
- [62] J. Esquivel, M.G. Wachowiak, S.P. O'Brien, R.K. Gupta, Thermal stability of nanocrystalline Al-5at%Ni and Al-5at%V alloys produced by high-energy ball milling, *J. Alloy. Compd.* 744 (2018) 651–657, <https://doi.org/10.1016/j.jalcom.2018.02.144>.
- [63] J. Esquivel, R.K. Gupta, Corrosion behavior and hardness of Al-M (M: Mo, Si, Ti, Cr) alloys, *Acta Metall. Sin. Engl. Lett.* 30 (2017) 333–341, <https://doi.org/10.1007/s40195-017-0550-2>.
- [64] J. Christudasjustus, T. Lariman, J. Esquivel, S. Gupta, A.A. Darwish, T. Borkar, R.K. Gupta, Aluminum alloys with high elastic modulus, *Mater. Lett.* 320 (2022), 132292, <https://doi.org/10.1016/J.MATLET.2022.132292>.
- [65] L. Vegard, The constitution of mixed crystals and the space filling of the atoms, *J. Phys.* 5 (1921) 17–26, <https://doi.org/10.1007/BF01349680>.
- [66] T. Uesugi, K. Higashi, First-principles studies on lattice constants and local lattice distortions in solid solution aluminum alloys, *Comput. Mater. Sci.* 67 (2013) 1–10, <https://doi.org/10.1016/j.commatsci.2012.08.037>.
- [67] B.D. Cullity, S.R. Stock, Elements of X-ray Diffraction, third ed., Pearson Education Limited, 2014.
- [68] A. Valério, S.L. Morelão, Usage of Scherrer's formula in X-ray diffraction analysis of size distribution in systems of monocrystalline nanoparticles, *Condens. Matter Mater. Sci.* (2019). (<http://arxiv.org/abs/1911.00701>) (Accessed 1 April 2020).
- [69] A.L. Patterson, The Scherrer formula for X-ray particle size determination (<https://journals.aps.org/pr/pdf/>), *Phys. Rev.* 56 (1939) 978–982, <https://doi.org/10.1103/PhysRev.56.978>.
- [70] F.T.L. Muniz, M.A.R. Miranda, C. Morilla Dos Santos, J.M. Sasaki, The Scherrer equation and the dynamical theory of X-ray diffraction, *Acta Crystallogr. A Found. Adv.* 72 (2016) 385–390, <https://doi.org/10.1107/S205327331600365X>.
- [71] L. Esteves, J. Christudasjustus, S.P. O'Brien, C.S. Witharamage, A.A. Darwish, G. Walunj, P. Stack, T. Borkar, R.E. Akans, R.K. Gupta, Effect of V content on corrosion behavior of high-energy ball milled AA5083, *Corros. Sci.* 186 (2021) 109–465, <https://doi.org/10.1016/j.corsci.2021.109465>.
- [72] L. Esteves, C.S. Witharamage, J. Christudasjustus, G. Walunj, S.P. O'Brien, S. Ryu, T. Borkar, R.E. Akans, R.K. Gupta, Corrosion behavior of AA5083 produced by high-energy ball milling, *J. Alloy. Compd.* 857 (2021) 158–268, <https://doi.org/10.1016/j.jalcom.2020.158268>.
- [73] V.B. Vukkum, J. Christudasjustus, A.A. Darwish, S.M. Storck, R.K. Gupta, Enhanced corrosion resistance of additively manufactured stainless steel by modification of feedstock, *Npj Mater. Degrad.* 6 (2022) 1–11, <https://doi.org/10.1038/s41529-021-00215-z>.
- [74] F. Ozdemir, C.S. Witharamage, A.A. Darwish, H. Okuyucu, R.K. Gupta, Corrosion behavior of age hardening aluminum alloys produced by high-energy ball milling, *J. Alloy. Compd.* 900 (2022), 163488, <https://doi.org/10.1016/J.JALLCOM.2021.163488>.
- [75] J.A. Moreto, C.E.B. Marino, W.W. Bose Filho, L.A. Rocha, J.C.S. Fernandes, SVET, SKP and EIS study of the corrosion behaviour of high strength Al and Al-Li alloys used in aircraft fabrication, *Corros. Sci.* 84 (2014) 30–41, <https://doi.org/10.1016/j.corsci.2014.03.001>.
- [76] L.B. Coelho, M. Hacha, Y. Paint, M.G. Olivier, Highlighting the effect of the aluminium alloy self-corrosion on the AA2024-T3/Ti6Al4V galvanic coupling in NaCl media, *Surf. Interfaces* 16 (2019) 15–21, <https://doi.org/10.1016/J.SURFIN.2019.04.004>.
- [77] T. Hashimoto, X. Zhang, X. Zhou, P. Skeldon, S.J. Haigh, G.E. Thompson, Investigation of dealloying of S phase (Al₂CuMg) in AA 2024-T3 aluminium alloy using high resolution 2D and 3D electron imaging, *Corros. Sci.* 103 (2016) 157–164, <https://doi.org/10.1016/J.CORSCI.2015.11.013>.
- [78] X. Zhang, T. Hashimoto, J. Lindsay, X. Zhou, Investigation of the de-alloying behaviour of 0-phase (Al₂Cu) in AA2024-T351 aluminium alloy, *Corros. Sci.* 108 (2016) 85–93, <https://doi.org/10.1016/j.corsci.2016.03.003>.
- [79] Z.F. Lodhi, W.J. Hamer, J.M.C. Mol, H. Terryn, J.H.W. De Wit, Galvanic compatibility of corrosion protective coatings with AA7075 aluminum alloy, *Mater. Corros.* 59 (2008) 306–310, <https://doi.org/10.1002/MACO.200804095>.
- [80] Y. Zou, Cold spray additive manufacturing: microstructure evolution and bonding features, *Acc. Mater. Res.* (2021), <https://doi.org/10.1021/ACCOUNTSMR.1C000138>.
- [81] M. Iannuzzi, T. Young, G.S. Frankel, Aluminum alloy corrosion inhibition by vanadates, *J. Electrochem Soc.* 153 (2006) B533, <https://doi.org/10.1149/1.2358843>.
- [82] M. Iannuzzi, G.S. Frankel, Mechanisms of corrosion inhibition of AA2024-T3 by vanadates, *Corros. Sci.* 49 (2007) 2371–2391, <https://doi.org/10.1016/j.corsci.2006.10.027>.